DOR: 20.1001.1.27170314.2021.10.3.8.1

Research Paper

An Investigation of Using RCS-processed Intramedullary Stainless Steel 316L Nail in the Treatment of Diaphyseal Bone Fractures

Abdolreza Rastitalab[1], Salar Khajehpour[1*], Ahmad Afsari[1], Shahin Heidari[2], Javad Dehghani[2]

[1]Department of Mechanical, Shiraz Branch, Islamic Azad University, Shiraz, Iran
[2]Bone and Joint Diseases Research Center, Shiraz University of Medical Sciences, Shiraz, Iran
[*]Email of Corresponding Author: khajehpour@iaushiraz.ac.ir
Received: August 12, 2021; Accepted: November 11, 2021

Abstract
The method of intramedullary nailing, which leads to the alignment of the diaphyseal broken bone, is one of the diaphyseal fractured bone healing novelties. The rods utilized must be strong enough to withstand the forces exerted by the transplanted bone. Today, various researchers are interested in using severe plastic deformation (SPD) methods to improve the mechanical characteristics of metals. One of the SPD procedures used in this study was repetitive corrugation and straightening (RCS) on a 316L stainless steel rod. After conducting mechanical characteristics tests on the rods produced using this approach, ABAQUS software was utilized to simulate the intramedullary nailing finite element method (FEM). The results of the experiments revealed that raising the number of pressing stages to eight significantly increases the hardness of the samples. The simulation findings revealed that the bone sample implanted by the rod manufactured by the aforementioned procedure has a higher structural hardness than the bone implanted by a basic 316L stainless steel rod under various stress conditions.

Keywords
Diaphyseal Bone Fractures, Intramedullary Nailing, SPD, RCS, Finite elements method

1. Introduction

Today, in innovative medicine, nail implantation techniques with the least amount of skin harm and the shortest period to rebuild a shattered bone are used. While using platinum and plaster to align fractured bones is not recommended due to several issues such as lingering surgery wounds, limitations in the patient's activity due to the presence of additional support around the fracture site, and the risk of the bone-inside screw and plaque breaking out [1].

The intramedullary nail is one of several orthopedic implants that are frequently used to treat long-bone fractures. One of the fracture healing treatments is intramedullary nailing, which is used to align the damaged bone. One of the most significant advantages of the intramedullary nail is the ease of surgery, the decrease of surgery time, and the reduction of skin and tissue irritation and rupture around the bone. Furthermore, embedding and removing the intramedullary nail is too simple for a surgeon,

and no external equipment is required; this is one of the reasons why this procedure causes less infection [2].

In this case, stainless steel external intramedullary nails of various diameters are created. Because of the loading on the nail, the lack of strength of the intramedullary nail is the most common cause of deformation and shortening of the bone during healing. Furthermore, the nail's lack of strength causes it to deviate and damage delicate tissues around the bone. It should be noted that in 27 percent of cases, deviation and damage cause pain and severe protuberance at the nail's intake. As a result, having a material with a high tensile strength capability is preferable [3].

In this regard, there are numerous research projects devoted to researching and enhancing the mechanical properties of metals. This is because of that this type of metal is commonly employed in the medical industry due to its unique properties [4].

With the advancement of the medical sector, it is becoming less necessary to strengthen the features of stainless steel alloys, such as high strength. Using the mechanical alloying technique, many researchers have attempted to generate high-strength stainless steel [5].

The biggest issue with this approach is the microscopic porosities and the possibility of cracking. Impurities, which aid in increasing crystal structure strength, and structural defects, such as grain boundaries and dislocations, play a significant and determinative role in the creation of strength in stainless steel [6].

Based on the scientific literature supplied, a method to improve the mechanical properties of high tensile strength stainless steel must be described and developed. Polycrystalline materials with very fine grading, such as nanometers and/or hundreds of nanometers (less than a micron), have piqued the curiosity of many researchers in the last two decades due to their unique mechanical and physical properties. The mechanical and physical properties of crystalline materials are influenced by a variety of factors, one of which is the medium grain size. The Hall-Petch relation states that the material's strength is proportional to the square inverse of grain size. In other words, decreasing the grain size enhances the material's strength [7].

$$\sigma_y = \sigma_0 + k_y d^{-\frac{1}{2}} \qquad (1)$$

Where depending on the material, _y is yield stress, _0 is lattice resistance, d is grain size, and k y is a constant. Severe plastic deformation (SPD) is one of the emerging production methods for nanometer-grain size materials. The size of grains in this process is reduced to the nanoscale by applying severe strains to the sample, resulting in a remarkable increase in the mechanical properties of metal. Because material dimension variations can obstruct the strain imposed, the majority of SPD procedures are designed to keep the sample dimensions constant throughout the process. Based on SPD, the production process of nanometer-grain size materials was explored in this study. These studies discovered a link between very fine grain refinement, a high volume fraction of grain borders, and exclusive polycrystalline deformation behavior under superplastic circumstances [8].

Today, materials with very small microstructures are generated by applying very large strains utilizing SPD techniques. Some of the SPDs are Equal Channel Angular Pressing (ECAP) and high-pressure Twist Extrusion (TE). All of these methods have one thing in common: they all keep the workpiece's dimensions constant during the deformation process. Another feature of these procedures is the improvement in material strength without the addition of alloying elements or ceramic particles;

of course, the production rate is quite low in these processes, and in most situations, high-capacity deforming equipment, and expensive molds are necessary. During the procedure, Repetitive Corrugation and Straightening (RCS) is one of the novel methods used [9].

In addition to manufacturing bulk nanostructure materials without contamination or porosity, this technology can be used to produce them on an industrial scale. The workpiece bends and flattens repeatedly in the RCS process with no discernible change in its cross-section area. There are two steps in the RCS process' main cycle. As a result, the material is subjected to a tremendous amount of plastic strain, which results in the formation of a very thin structure [10].

The steel industry is constantly developing new high-strength steels, which are referred to as advanced steels. This is because of higher tensile strength, more appropriate plasticity, more suitable toughness all of which are obtained through improving microstructure [11].

The Transformation induced Plasticity Steel (TRIP) is attributable to the transformation of unstable retained austenite to martensite during deformation at the ambient temperature. This characteristic of TRIP steels allows having both plasticity and high strength [12].

The modified-properties steel presents a fascinating combination of flexibility and tensile strength. In conclusion, to prevent deformation and damage to the bone, these steels can be a very suitable substitution for intramedullary nailing [13].

In this research, the RSC process was used to create severe deformation plastic in the rods made of stainless steel. Hence, using the RCS process and SPD, the compressive strength of the nails used to implant in a fractured bone increases so that the implanted bone endures more applying forces. Using the finite element method (FEM) to achieve more stability, the arrangement of the implant model (C-shape) under a compressive loading was simulated for both materials, and the results obtained were analyzed.

2. Materials and Method

2.1 Initial substance

In this research, 316L stainless steel was utilized to reform the fractured bone. Stainless steel is one of the biological materials, which are often used for body-inside implants, because of a suitable combination of mechanical properties, corrosion resistance, and affordability compared to the other materials. This metal is a stainless alloy, consisting of austenitic chromium, nickel, and molybdenum, which resists well against corrosion. This steel is obtained based on some modifications like adding chromium and reducing carbon. Low carbon content decreases sedimentation of chromium carbide, which will have a direct influence against grain boundary corrosion [14].

The lack of a magnetic characteristic implies that these alloys are non-magnetic due to their austenitic matrix and structure. Austenite is a body-centered cubic (BCC) iron phase that is stable in iron without alloying elements at temperatures ranging from 910°C to 1400°C. Austenite can be made to be stable at room temperature by adding austenitic elements such as nickel. The alloy's mechanical properties, notably its plasticity, alter as a result of the phase transition. These alloys are non-magnetic in tempered conditions due to the austenite phase, however, a small magnetic characteristic can be obtained due to phase shift in the cold work state. The chemical composition of 316L stainless steel was determined using spark emission spectroscopy (SES) and compared to the ASTM A240 standard [15], as shown in Tables 1 and 2.

Table 1. The 316L stainless steel's mechanical properties

Vickers hardness	Elongation mm 50 (%)	Yield stress(MPa)	Ultimate tensile strength (MPa)
155	60	205	515

Table 2. The chemical compound of 316L used for WT %

Element	Fe	Si	P	N	C	S	Mn	Mo	Ni	Cr
Weight percent	base	0.75	0.045	0.1	0.03	0.03	2	2.5	12	17
Weight percent [15]	base	0.75	0.045	0.1	0.03	0.03	2	3-2	14-10	18-16

2.2 Implant rod rolling equipment used in a repeating corrugation and straightening procedure

Two continuous and discontinuous moulds undertake the repeating corrugation and straightening procedure. The continuous mould was used in this study to meet the manufacturing requirements on an industrial scale. Squeezing the corrugated workpiece between two rollers achieves straightening. Two grooved rollers and two straightening rollers made of AISI 1.6580 tool steel were chosen and machined according to the plan before being heat treated. The mold was treated with solution operations at 860°C for 80 minutes, including annealing, stress relief, and hardening, before being cooled in an oil medium for quenching. Tempering was also done for 180 minutes at three different temperatures: 210°C, 360°C, and 460°C resulting in a 50 RC hardness in the mold [16].

2.3 The corrugation and straightening operation is repeated several times

They were heat-treated according to the ASTM standard A1021/A1021M-05 to relieve residual tensions and increase the strength and hardness of the 316L stainless steel [17]. The samples were heated for 60 minutes at 1000°C before being cooled in water. The technique was carried out at a strain rate of 10-3 s-1 at 200°C to prevent the creation of the martensite phase in the 316L stainless steel alloy samples during the recurrent corrugation and straightening process, as well as a high density of dislocations in the austenite phase. An electric heater was installed in the mold to keep the process warm [18]. To make a required isotherm, the samples were first placed in a furnace for 5 minutes at a previously attained desired temperature. After one phase of corrugating and straightening, the sample was turned 90° clockwise along the longitudinal axis and placed in the grooved roller to distort the entire sample during corrugating and straightening. MoDTC (a chemical lubricant) was used to lubricate the grooves of the mould and the sample before the experiment to reduce friction between the surfaces of the mould and the sample [19] (Figures 1 and 2).

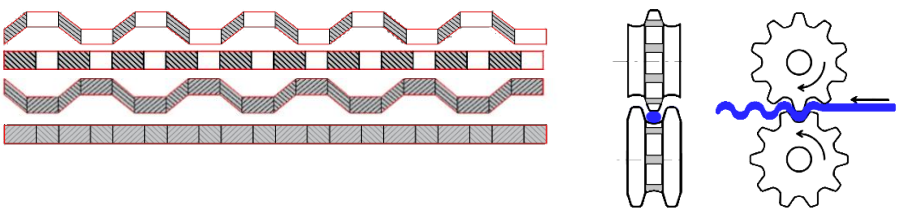

Figure 1. Shows a diagram of the RCS process

2.4 Microstructure investigation

An IEI- IMM420 optical microscope was used to examine the cross-section microstructure of 316L stainless steel that had been processed via serial corrugation and straightening. Furthermore, an Explorer X-Ray Diffraction (XRD) built by GNR was used to examine the chemical composition, morphology, and grain size of the samples and the peaks were analyzed using ORIGIN software.

Figure 2. RCSed stainless 316l sample drawing

2.5 Tension-Testing

All of the samples were prepared for the tension test according to the ASTM E8/E8M-16a standard and cut to the correct dimensions using a wire-cut machine. For all of the samples and the base metal, the tension test was carried out at a constant speed of 1 mm/min at room temperature [20].

2.6 Microhardness test

The Vickers criterion was used to conduct the microhardness test, which was done with a diamond square cross-section indenter, as per the ASTM E384-99 standard. To finish, the indenter tip was placed at 5 mm intervals on the cross-section middle line of the metallographic samples. A hardness tester (model D.H.V-1000) applied a 30 N force for 9 seconds, and the hardness fluctuations were displayed for different samples [21].

2.7 Elastic implant rod made through a process of corrugation and straightening

The C-shaped elastic model was used as the implant rod in the bone with a middle fracture in this study. Using a wire-cut machine, the initial and manufactured samples were cut to a length of 300 mm in the eighth pass to create this nail [22]. This rod has a diameter of 3 mm, and two sides of the rod were ground for finishing after the samples were cut and the machining operation was completed.

2.8 Pre-bent elastic rod inserted in a bone with an intermediate fracture simulation

The simulation of a pre-bent elastic rod implanted in a bone with a middle fracture was explored using ABAQUS software in this study, depending on the rod's geometry. The dimensions of the bone were long, according to CT images collected in one of Shiraz's hospitals of a healthy male (weight: 84 kg, height: 173 cm). A simple direct tube in the shape of an intramedullary channel with an inner diameter of 24 mm, an exterior diameter of 35 mm, and a length of 260 mm was considered to ease the problem of the bone shattered. To investigate the stability of the bone fractures, two elastic rods were simulated: a standard 316L stainless steel and a 316L stainless steel generated by the recurrent corrugation and straightening procedure. Two flexible rods with a 3 mm diameter and a 300 mm length were embedded in the pre-bent form through two 4 mm holes slightly below the bone's growth plane after the bone was designed. Figure 3 shows a simulation of an elastic rod constructed of 316L stainless steel implanted in a bone with a central fracture. Pre-bending, for example, is a typical approach used by orthopedic surgeons to increase the strength of the bone by increasing the amount

of surface contact between the rod and the bone. This is done without any scientific justification, even though the actual value of the pre-bending radius, as well as the rod's bending site, are unknown. However, by offering a rational answer, this difficulty can be handled [23-25]. The broken bone's strength was then investigated in a dynamic explicit manner using a FEM of the fractured bone and two flexible rods of varying strengths under the impact of axial and lateral loads. It should be noted that throughout the geometry construction, a simplification was carried out. 2 mm quadrangular components were used to mesh the bone, and 1.5 mm triangular elements were used to mesh two flexible rods [26].

The loading is less than a usual walking procedure due to the bone fracture and the need for supplementary protection; this was taken into account in our investigations. On the perpendicular plane, a 150 N axial pressure load and a 150 N flexural force were applied at a rotation angle of 10°. Furthermore, in the simulation, the muscle force was neglected. In the simulation procedure, a restricted provision was used, with one end of the bone locked and the other regarding free. All parts' connections were treated as surface-to-surface contacts for a more realistic simulation, and the coefficients of friction between metal and metal and metal and bone were set to 0.2 and 0.3, respectively [27, 28]. Figures 4 and 5 show how to mesh, load, and embed an elastic rod constructed of 316L stainless steel. The material features of the bone, which is a sort of composite tissue, are similar to a simple direct tube in this study, according to the investigations completed and recommendations offered in the literature. Bone is a linear elastic material, with an elastic modulus of 17 GPa and a Poisson's ratio of 0.3, respectively. The elastic modulus and Poisson's ratio for the elastic rod are shown in Table 3. [29] All materials are simplified to be isotropic and homogeneous. The goal is to increase the strength of the stainless steel rod using an SPD process with the smallest possible dimension deviations (Figure 3).

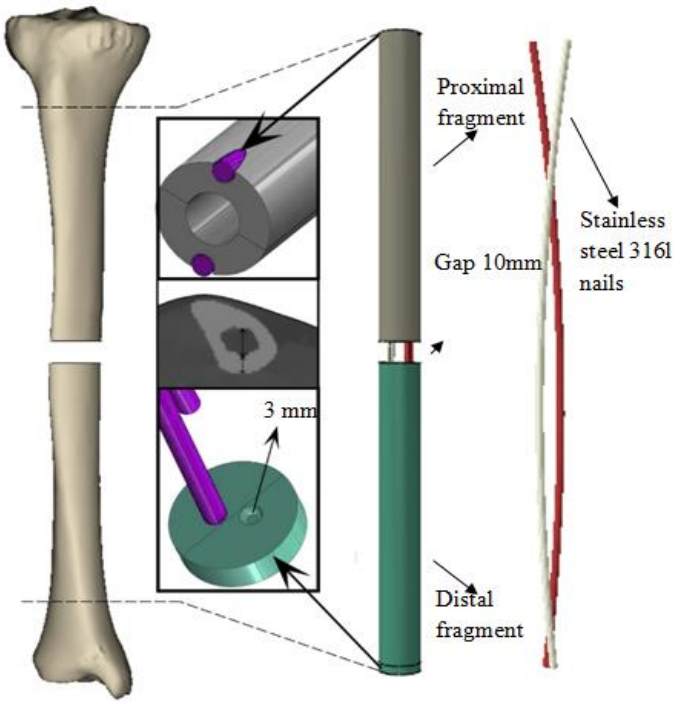

Figure 3. An implant simulation of a 316L (RCSed) stainless steel elastic rod in a bone with a diaphyseal fracture

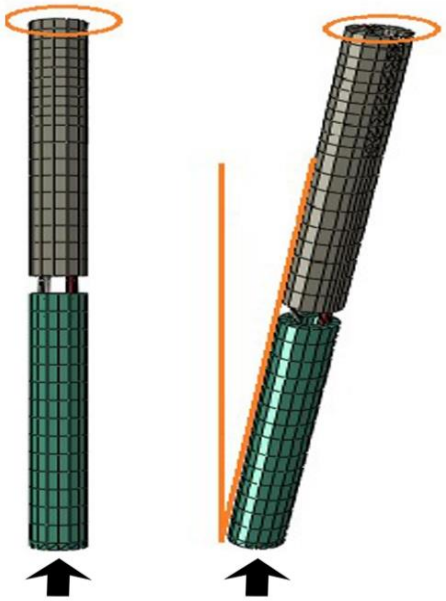

Figure 4. A FEM simulation of a nail and a bone under load

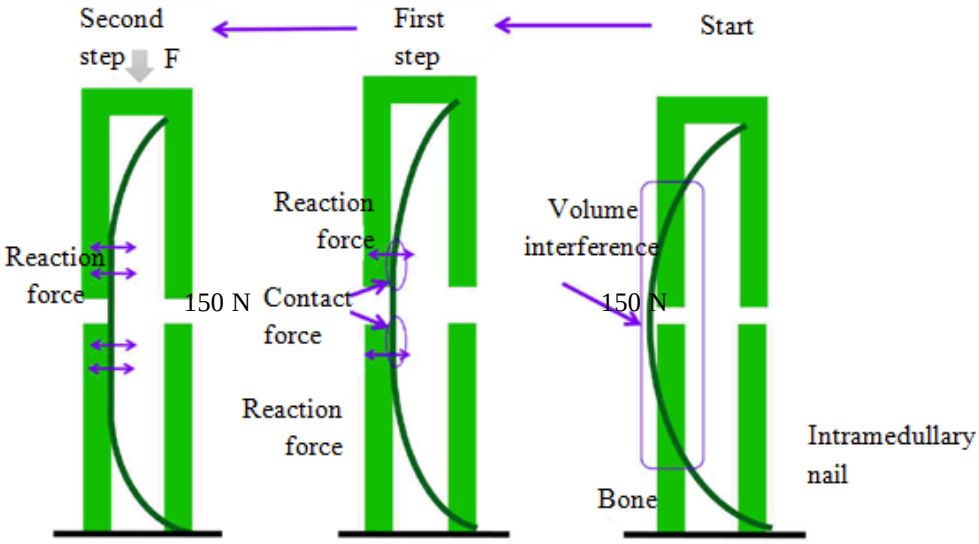

Figure 5. Intramedullary nails implanted into bone

Table 3. Shows the mechanical parameters of the elastic rods that were implanted.

Mechanical property	RCSed nail	Not RCSed nail
Hardness Vickers	468	155
(MPa) Ultimate stress	856	515
(MPa)Yield sress	453	205
(GPa) Young's Modulus	624	193
Poisson's ratio	0.25	0.3

2.9 The validation of the results

The current study's findings were compared to those obtained by Lin et al. [14]. They found a cylindrical tube with a length of 260 mm, an outside diameter of 260 mm, and a wall thickness of 11 mm, and constructed a 10 mm middle crack in the tube's core. The tube was then filled with two C-shaped elastic rods having a diameter of 3 mm. 316L stainless steel rods with a length of 300 mm were chosen. To locate the rods, holes were drilled using a 4mm drill underneath the tube. Furthermore, the holes were positioned at a 45° angle to the cylindrical tube's longitudinal axis to create an axial compressive force. The tube's lower end remained constant. The loading rate was set to one millimeter per minute.

Because both results have extremely comparable values, the results of the fractured bone model and the FEM elastic rod against the stiffness of the axial pressure in this study confirm the results of the experimental study under identical conditions. Despite the advantages mentioned for numerical modeling, experimental studies and models have their limitations in presenting how to operate the fractured bone with the flexible rod and its problems [30]. These results are usable for a biomechanical condition of a specific population due to an investigation on the sensitivity of the parameters and the modeling of medical implants. Figures 6a and b show a comparison of the FEM elastic rod's axial compressive stiffness with the results of the experimental research.

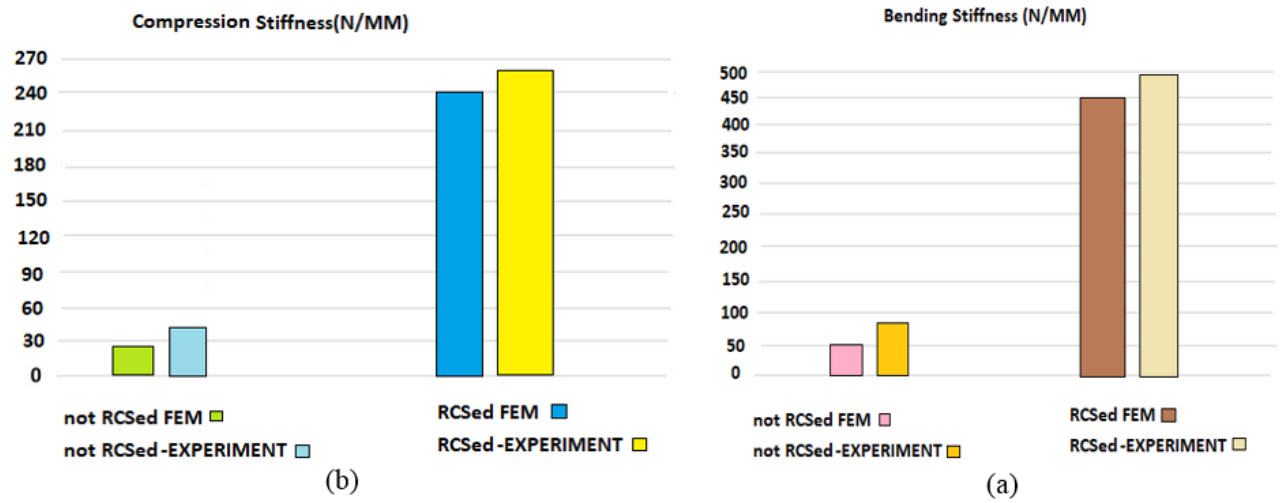

Figure 6. Experimental data versus FEM elastic rod (a) axial compression stiffness and (b) flexural stiffness

3. Results and Discussion

3.1 Analysis of microstructure

The optical microscope image of the first elastic rod's wire-cut surface is shown in Figure 7. Coarse grains may be seen in this image. According to the criteria deviation method, the average range of grain size of this microstructure is 35 nm. The structure of the samples gets drastically finer after the repeated corrugation and straightening procedure resulting from applying strain in each phase. The repeated corrugation and straightening procedure after the eighth pass resulted in finer grains, resulting in a hard estimate of grain size (Figure 7). The peaks acquired from various steps of the repeating corrugation and straightening procedure are shown in Figure 8. The peak height decreases as the number of deformation steps increases, as can be seen. The findings show that when the strain

caused by the repeated corrugation and straightening process increases, the grain size decreases. For various steps of the recurrent corrugation and straightening process, Figure 8 displays varied grain size values determined using the Williamson-Hall method. The grain size of the investigated samples was determined using X-ray diffraction examination. The peaks associated with each plane were first separated, and the index of planes was determined to examine the X-ray diffraction results. The peaks corresponding to each of the differentiation planes in which the intensity of the reflected beam is in terms of 2 were then determined using ORIGIN software (Figure 8).

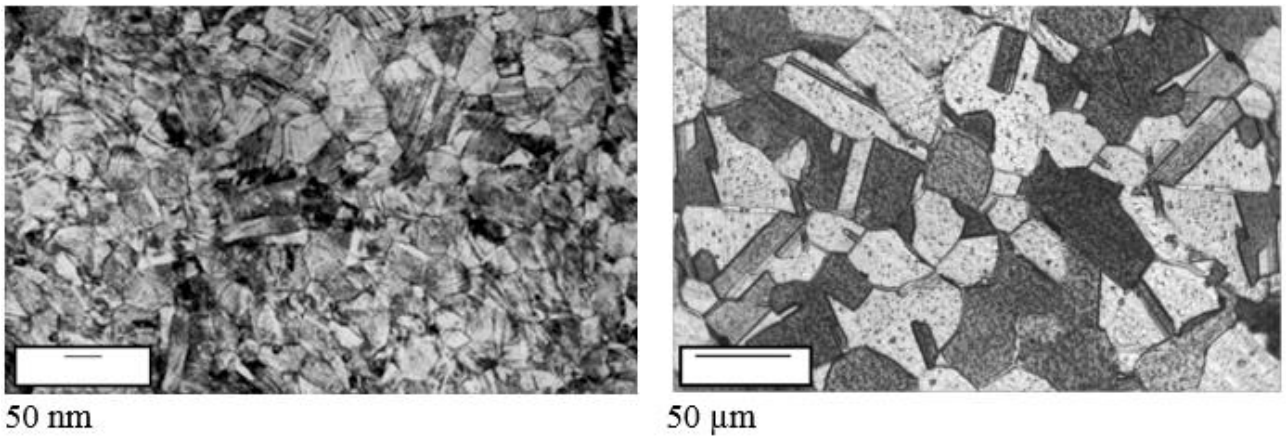

Figure 7. RCSed intramedullary nail cross-section viewed via an optical microscope

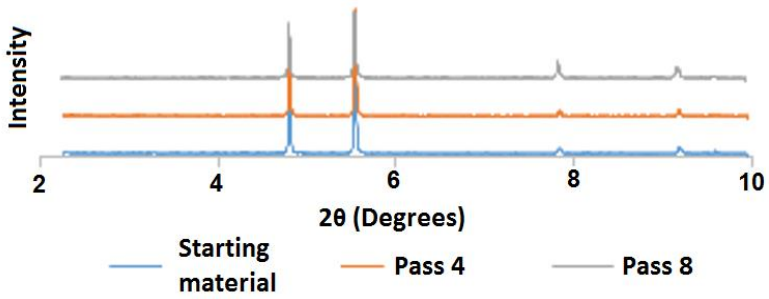

Figure 8. RCSed nail X-ray diffraction patterns

3.2 Hardness test

Figures 9 and 10 depict sample hardness fluctuations as a function of the number of steps and hardness values in terms of longitudinal distance from a sample edge, respectively. The hardness of 316L stainless steel is almost 159 V, as shown in Figure 9; following the first, fourth, and eighth passes of the recurrent corrugation and straightening process, this value reaches 248, 255, and 284 V, respectively. It's worth noting that the initial pass's hardness is increasing rapidly, and this trend is expected to continue as the number of passes increases. The hardness uniformity is increased by the mechanical properties uniformity as the number of passes of the repeating corrugation and straightening process rises (Figures 9 and 10).

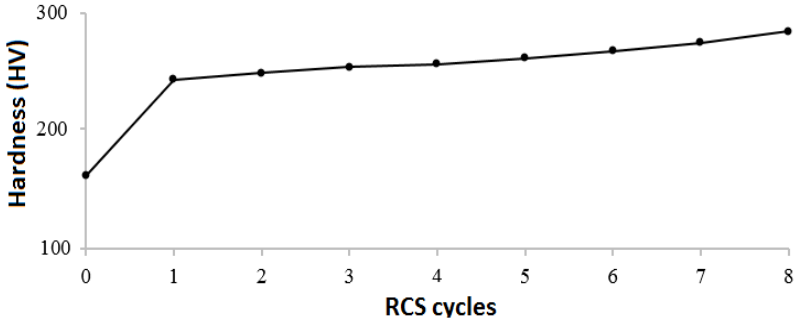

Figure 9. Hardness variation as a function of RCS cycles

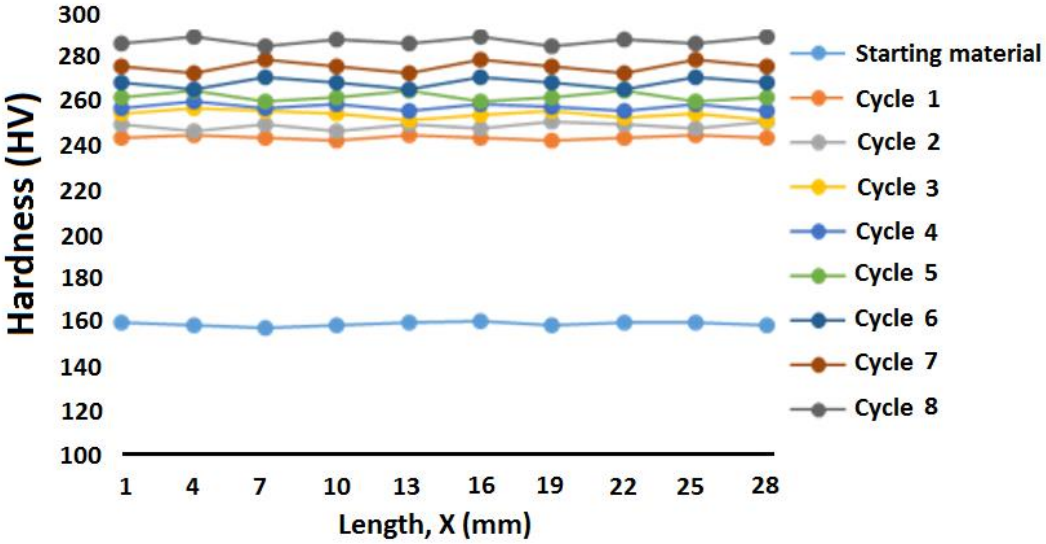

Figure 10. Hardness variation across sample cross-sections during RCS passes

3.3 Results of tensile strength

Figure 11 depicts the variations in yield strength, tensile strength, and elongation for the samples produced by the RCS operation in terms of the number of passing steps, as determined by the single-axis tension test for the initial sample and the samples produced by the RCS process from step one to step eight. The yield strength in the first pass improves from 258 MPa to 480 MPa, as can be shown. Furthermore, the compressive strength rises to 586 MPa from 515 MPa (Figure 11). Because the workpiece's ultimate strength in the eighth pass is lower than in the first, it has elastic qualities even after the eighth pass.

In the first pass, the percentage elongation drops by up to 64%. This is due to yield and compressive strength values calculated utilizing SPD and based on grain size fineness.

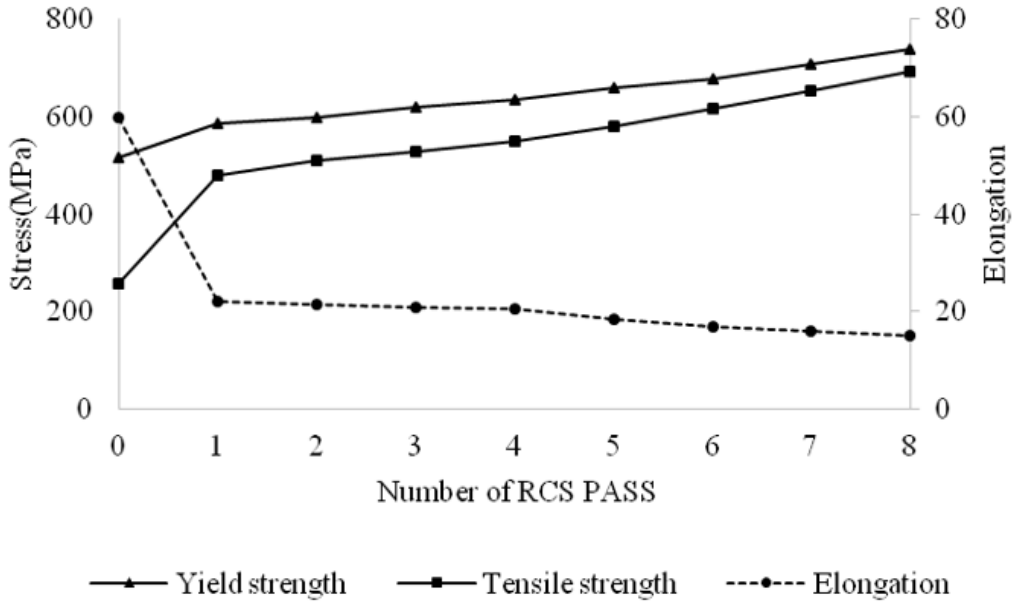

Figure 11. Yield strength, tensile test, and elongation variations during several RCS pass

3.4 Results of simulation

Four forms of meshing with different cells were used in this study to provide numerical findings independent of meshing, and the stress rate begun by the flexural force in the elastic rod was chosen as the independent studying parameter from meshing. The meshing results of the simulation, as shown in Table 4 are 131925 nodes and 79852 elements.

Table 4. Mesh refinement study

Error % compared to the previous mesh refinement	Stress(MPa)	Number of elements
------	87.8	45.69
10.8	89.1	75.18
5.6	91.9	123.3
1	92.6	154.53

One of the most important benefits of this study is the scientific study and simulation of elastic steel rods, one of which is a simple 316L stainless steel and the other is 316L stainless steel produced by the RCS process in the intramedullary channel, on which no scientific research has been done. The originality of developing a steel elastic rod with modified material results in increased strength as well as elasticity, resulting in improved rod pre-bending quality and, as a result, the use of small diameter rods. As a result, surgery is made easier, and the cost of transverse fractures within the bone channel is decreased.

The amount of deformation, Von Mises stresses induced in the bone and rod, and the contact force between the bone and the rod are all part of the findings of this study. The rods are pre-bent three times the diameter of the bone canal, according to research. Furthermore, the cap secures the rods' ends, resulting in improved stability against compressive and flexural forces [31]. The eighth pass of the repeating corrugation and straightening procedure achieved the greatest hardness in the 316L stainless steel rod (Table 5).

Table 5. RCSed versus non-RCSed nail structural stiffness comparison

Error % compared to the previous mesh refinement	Stress (MPa)	Number of elements
------	87.8	45.69
10.8	89.1	75.18
5.6	91.9	123.3
1	92.6	154.53

3.5 Deformation of nails and gaps

The simulation findings revealed that the deformation in the arrangement of the 316L stainless steel rod produced by the repeating corrugation and straightening process in the eighth pass is less than the plain 316L stainless steel rod when subjected to bone pressure. The center of the bone and the intake part of the rods into the channel have the highest stress distribution in the 316L stainless steel rod implant created by the repeating corrugation and straightening process in the eighth pass (Figures 12 and 13).

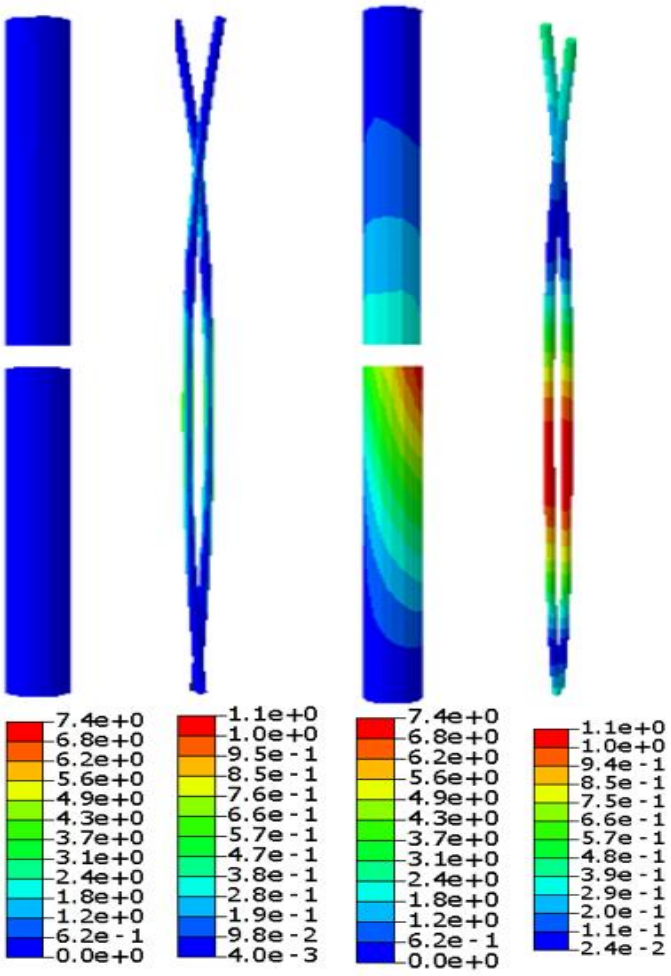

Figure 12. Compression deformation of RCSed and non-RCSed nails in millimeters a) RCSed nail b) not RCSed nail

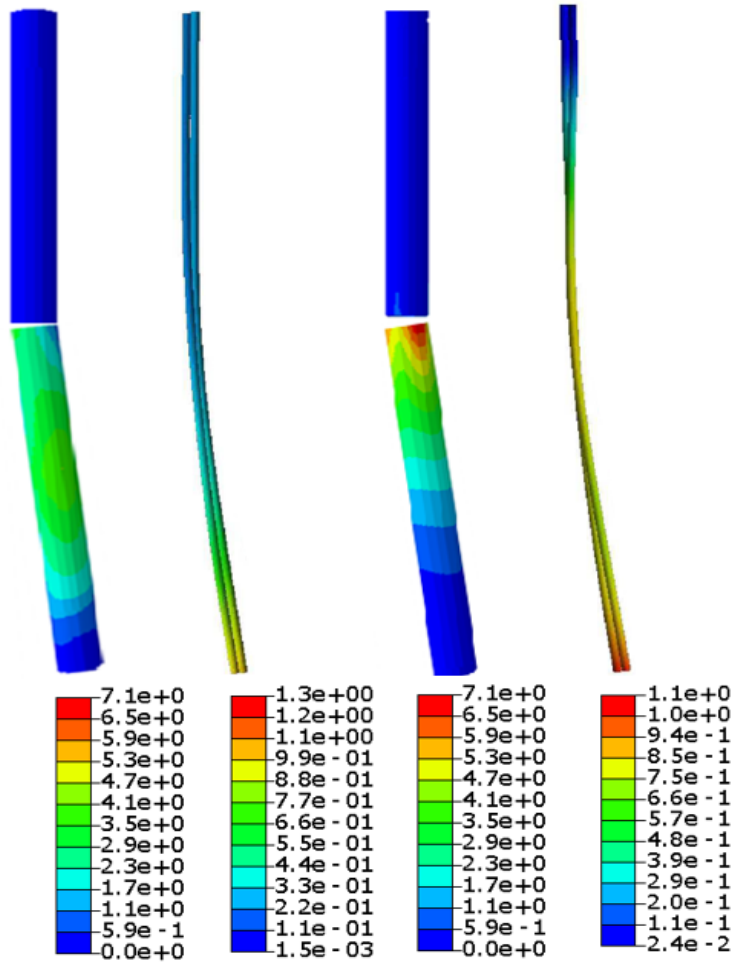

Figure 13. Shows the bending deformation of RCSed and non-RCSed nails in millimeters a) RCSed nail b) not RCSed nail

3.6 Von Mises tensile tension on an elastic rod

The rods show signs of excessive stress at the central axis and the middle of the fragmented bone. The 316L stainless steel rod generated by the repeating corrugation and straightening process in the eighth pass is more stable under axial compression stress than the plain 316L stainless steel rod (Figure 14).

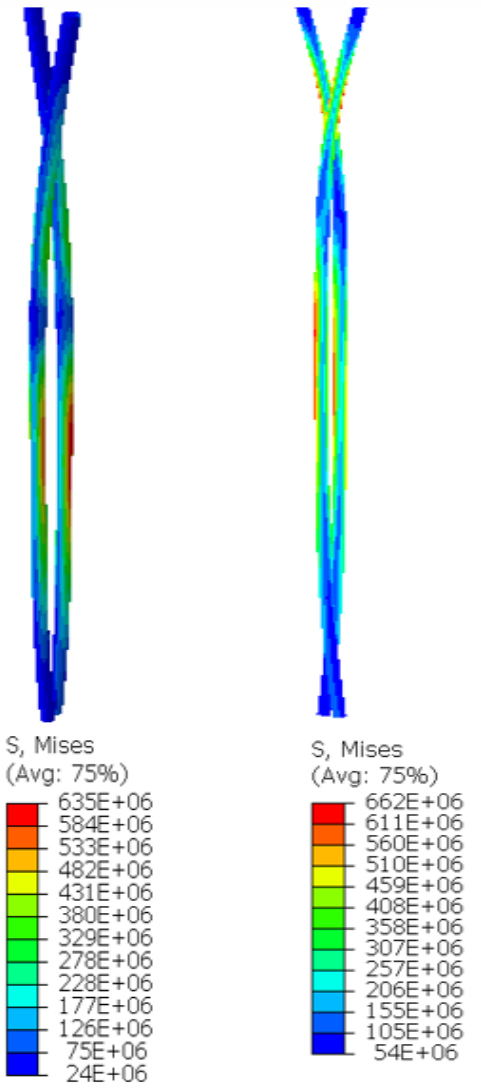

Figure 14. The Von Mises stresses (MPa) in RCSed and non-RCSed nails when they are compressed

3.7 The force at which the bone and the nail come into contact

In comparison to the 316L stainless steel rod, the resistance to deformation in the eighth pass implantation of the 316L stainless steel nail produced by the repeating corrugation and straightening process is higher. As a result, more friction is created, and so the contact force is increased (Table 6).

Table 6. Nail-to-cortical bone contact force (N)

	Not RCSed stainless steel 316l		RCSed Stainless steel 316l	
	Distal	Proximal	Distal 2	Proximal 1
Compression Force	7	115.1	27.5	297.4
Bending Force	4.8	111.5	16.7	297

[1] Proximal
[2] Distal

4. Conclusion

The compressive strength of the 316L stainless steel rod to implant in the broken bone was studied in this study, which involved an RCS process to produce SPD. Furthermore, simulation was used to compare the biomechanical behavior of these rods in terms of flexibility and strength while enduring the produced compressive stresses on the cracked bone. The mechanical qualities of the 316L stainless steel rod made by the repeating corrugation and straightening procedure in eight phases were considerably improved, according to the research findings. The structural hardness of the 316L stainless steel rod produced by the repeating corrugation and straightening process in the eighth pass is higher under different loadings (compressive and flexural) than the 316L stainless steel rod, according to the simulation results. When compared to a regular 316L stainless steel rod, the deformation under the influence of pressure and bending in the 316L stainless steel rod produced by the RCS process in the eighth pass is lower; this was one of the focus points in changing the rod's properties. Because of mechanical properties available in the 316L stainless steel rod produced by the RCS process during pre-bending of the rod, the contact force between the 316L stainless steel rod produced by the RCS process and the bone was higher than a regular 316L stainless steel rod and the bone. There were some limitations to this investigation. A model with bone and rod was created to facilitate the analysis of the FEM. Soft tissues, such as muscles and ligaments, were, nevertheless, overlooked. The bone was reduced to a single, straight tube. The uneven shape of the passage inside the bone was also eliminated to simplify the geometry. Because of the irregularity of the channel and the inner mechanical response like stress and strain between genuine bone and stress and strain in the current tube model, the contact situation between the channel of a real bone and the nail was more problematic. Furthermore, only partial forces of body weight were taken into account. The muscular force and the stress caused by ligaments were not taken into account. In clinical practice, a fractured bone should be protected immediately after surgery. Furthermore, even after the bone has been fused with a rod, modest weight-bearing is usually recommended. As a result, the loading conditions chosen in this study were solely to evaluate the fractured bone's strength, which does not include the strength following callus (bone inner membrane) creation.

5. References

[1] Srivastava, A.K., Mehlman, C.T., Wall, E.J. and Do, T.T. 2008. Elastic stable intramedullary nailing of tibial shaft fractures in children. Journal of Pediatric Orthopaedics. 28(2): 152-158.

[2] Rastitalab, A., Khajepour, S., Dehghani, J., Afsari, A. and Heidari, S. 2021. Evaluating the Stability of the Fractured Bone Implanted with Titanium Elastic Nails in C and S Configurations. Journal of Hunan University Natural Sciences, 48(9):349-358.

[3] Perren, S.M. 1989. The biomechanics and biology of internal fixation using plates and nails. Orthopedics. 12(1):21-34

[4] Chen, X.H., Lu, J., Lu, L. and Lu, K. 2005. Tensile properties of a nanocrystalline 316L austenitic stainless steel. Scripta Materialia. 52(10): 1039-1044.

[5] Bakhshan, Y., Heidari, S., Khorshidi, J. and Afsari, A. 2021. Study of Aerodynamic Parameters of WAF and Flat Fins Rocket with Two Materials of Aluminum & Steel and Its Effect on Elastic Deformation by Two-way FSI Method. Journal of Mechanical Engineering. Available Online. 10.22034/jmeut.2021.42557.2774.

[6] Afsari, A., Heidari, S. and Jafari, J. 2020. Evaluation of Optimal Conditions, Microstructure, and Mechanical Properties of Aluminum to Copper Joints Welded by FSW. Journal of Modern Processes in Manufacturing and Production. 9(4): 61-81.

[7] Heidari, S. and Afsari, A., 2021. Study of Mechanical Properties of 7075 Aluminum Alloy Due to Particle Size Reduction due to Constrained Groove Pressing CGP Process. Journal of Modern Processes in Manufacturing and Production, 10(1): 5-18.

[8] Heidari, S., Afsari, A. and Ranaei, M.A. 2020. Increasing Wear Resistance of Copper Electrode in Electrical Discharge Machining by Using Ultra-Fine-Grained Structure. Transactions of the Indian Institute of Metals. 73(11): 2901-2910.

[9] Tahavvor, A.R., Heidari, S. and Zarrinchang, P. 2016. Modeling of the height control system using artificial neural networks. Journal of Agricultural Machinery. 6(2): 350-361.

[10] Orang, A., Haghighi-Yazdi, M., Naserkhaki, S. and Mehrpour, S.R. 2020. Desired Properties of Disc in Numerical Models and Its Influence on Biomechanical Behavior of Lumbar Spine. Amirkabir Journal of Mechanical Engineering. 52(1): 87-202.

[11] Tahavvor, A.R. and Zarrinchang, P. 2020. Numerical simulation of transient air flow and particle deposition in a lung and bronchus of a human respiratory system. AUT Journal of Mechanical Engineering. 4(3): 347-362.

[12] Pham, M.S., Dovgyy, B. and Hooper, P.A. 2017. Twinning induced plasticity in austenitic stainless steel 316L made by additive manufacturing. Materials Science and Engineering: A. 704:102-111.

[13] Sudhakar, K.V. 2005. Metallurgical investigation of a failure in 316L stainless steel orthopaedic implant. Engineering Failure Analysis. 12(2): 249-256.

[14] Liu, G., Li, J., Zhang, S., Wang, J. and Meng, Q. 2016. Dilatometric study on the recrystallization and austenization behavior of cold-rolled steel with different heating rates. Journal of Alloys and Compounds. 666: 309-316.

[15] ASTM A 167 or ASTM A 240/A 240M. Type [304][316][304 or Type 316].

[16] Chandler, H. 1995. Heat treater's guide: practices and procedures for irons and steels. ASM International.

[17] Tupholme, S. 1990. Information Sources in Metallic Materials. Chapter Four: Stainless steels. KG Saur.

[18] Yanushkevich, Z., Dobatkin, S.V., Belyakov, A. and Kaibyshev, R. 2017. Hall-Petch relationship for austenitic stainless steels processed by large strain warm rolling. Acta Materialia. 136: 39-48.

[19] Wang, Y., Yue, W., She, D., Fu, Z., Huang, H. and Liu, J. 2014. Effects of surface nanocrystallization on tribological properties of 316L stainless steel under MoDTC/ZDDP lubrications. Tribology International. 79: 42-51.

[20] Wang, P., Lei, H., Zhu, X., Chen, H. and Fang, D., 2019. Influence of manufacturing geometric defects on the mechanical properties of AlSi10Mg alloy fabricated by selective laser melting. Journal of Alloys and Compounds, 789, pp.852-859.

[21] ASTM E384-99-Standard Test Method for Microindentation Hardness of Materials. 1999. ASTM International West Conshohocken.

[22] Kim, J.Y., Cho, S.I., Lee, I., Na, H.J. and Jung, S.Y. 2012. Aerodynamic analysis of a rolling wraparound fin projectile in supersonic flow. International Journal of Modern Physics: Conference Series. 19: 276-282.

[23] Goodwin, Ryan C. Gaynor, T., Mahar, A., Oka, R. and Lalonde, F. D. 2005. Intramedullary flexible nail fixation of unstable pediatric tibial diaphyseal fractures. Journal of Pediatric Orthopaedics. 25(5):570-576.

[24] Ligier, J.N., Metaizeau, J.P., Prevot, J. and Lascombes, P. 1985. Elastic stable intramedullary pinning of long bone shaft fractures in children. Zeitschrift für Kinderchirurgie. 40(4): 209-212.

[25] Anderson, R.T., Pacaccio, D.J., Yakacki, C.M. and Carpenter, R.D. 2016. Finite element analysis of a pseudoelastic compression-generating intramedullary ankle arthrodesis nail. Journal of the Mechanical Behavior of Biomedical Materials. 62: 83-92.

[26] Ariza, O., Gilchrist, S., Widmer, R.P., Guy, P., Ferguson, S.J., Cripton, P.A. and Helgason, B. 2015. Comparison of explicit finite element and mechanical simulation of the proximal femur during dynamic drop-tower testing. Journal of Biomechanics. 48(2): 224-232.

[27] Shirazi-Adl, A., Dammak, M. and Paiement, G. 1993. Experimental determination of friction characteristics at the trabecular bone/porous-coated metal interface in cementless implants. Journal of Biomedical Materials Research. 27(2): 167-175.

[28] Kaiser, M.M., Zachert, G., Wendlandt, R., Eggert, R., Stratmann, C., Gros, N., Schulze-Hessing, M. and Rapp, M. 2012. Increasing stability by pre-bending the nails in elastic stable intramedullary nailing: a biomechanical analysis of a synthetic femoral spiral fracture model. The Journal of Bone and Joint Surgery. 94(5): 713-718.

[29] Gervais, B., Vadean, A., Raison, M. and Brochu, M. 2016. Failure analysis of a 316L stainless steel femoral orthopedic implant. Case Studies in Engineering Failure Analysis. 5: 30-38.

[30] Lee, P.Y., Chen, Y.N., Hu, J.J. and Chang, C.H. 2018. Comparison of mechanical stability of elastic titanium, nickel-titanium, and stainless steel nails used in the fixation of diaphyseal long bone fractures. Materials. 11(11): 2159.

[31] Chen, Y.N., Lee, P.Y., Chang, C.W., Ho, Y.H., Peng, Y.T., Chang, C.H. and Li, C.T. 2017. Biomechanical investigation of titanium elastic nail prebending for treating diaphyseal long bone fractures. Australasian Physical and Engineering Sciences in Medicine. 40(1): 115-126.